

BRIDGING RAY TRACING AND WAVE OPTICS: A COMPUTATIONALLY EFFICIENT MODEL FOR DEFOCUS AND SPHERICAL ABERRATION

Nicholas Ganino, Qi Guo

The Department of Electrical and Computer Engineering
Purdue University
West Lafayette, IN

ABSTRACT

The computation of the point spread function (PSF) of an optical system is a critical step in image signal processing. When it becomes necessary to determine the PSF for many smaller regions within an image or for multiple images taken in rapid succession, such as in live processing, the computation time can be a limiting factor. Additionally, modeling PSFs with common aberrations such as defocus or spherical often complicates results. This paper presents a computationally efficient mathematical model for determining the PSF of a system given the pupil function and the strength of the defocus aberration. Through approximations made in the Fourier transform derivation of the pupil function we develop a closed form solution for the PSF enabling 2D time complexity of $O(n^2)$ over the commonly implemented 2D FFT $O(n^2 \log n)$. We illustrate the validity of the approximations made in the derivation within a range of defocus strength and spatial extent. We also propose an extension of our method to be used for spherically aberrated PSFs. These results have the potential to accelerate image processing, especially in live-scene capture and may serve as a starting point for future work in non radially symmetric aberration analysis.

Index Terms— PSF, defocus, aberration

1. INTRODUCTION

With robotics, medical imaging, self-driving cars, and other real-time computer vision applications demanding rapid processing of live scenes [1], the need to decrease image computation time is key for future technology. Numerous computer vision techniques, especially those aiming to gain scene depth information or perform image restoration, rely heavily on the analysis of the Point Spread Function (PSF) of an optical system. The PSF of an imaging system is the image of a singular point source located in the object plane [2][3]. Despite ideally being a small bright point that mirrors the infinitesimal nature of a point source, the PSF typically takes on a larger shape, smearing across several pixels as a result of motion blur, defocus, or optical aberrations [4]. Also called the blur kernel, the PSF acts as the convolutional kernel of a spatially

invariant imaging system such that the detected image is the convolution of the ideal, perfectly imaged scene with the PSF. For this reason, determining the PSF is also an indispensable step in image signal processing (ISP), especially in denoising or deblurring methods. Furthermore, for systems with spatially varying blur, the number of PSFs that must be computed for a single image can grow dramatically. These ubiquitous cases in ISP and computer vision emphasize the need for faster methods of processing and computation, starting with the PSF.

There are two primary methods of determining the PSF of an optical system given the aperture size and object and sensor location, each on a different tier of accuracy and computational complexity. The first is based on the Huygens-Fresnel principle, where the PSF is found through rigorously ray-tracing points on the aperture, and the second is through Fraunhofer diffraction and the analysis of planar wavefronts in far-field propagation. In the former, each point on the aperture plane is treated as the source of an expanding spherical wave that impacts every point on the sensor plane. Then, the field strength at a single point on the sensor plane can be computed through the superposition of the total phase and amplitude incident from the sources on the aperture plane. This technique yields results with strong accuracy, as it considers the propagation of the fields from a large number of sources across your aperture and maintains the spherical wavefronts of point sources. However, since the value at each point on the sensor requires the summation of field values originating from each point source on the aperture, the computational cost of determining the PSF with this method is high at $O(n^2)$ for a one-dimensional system.

The second method employs the Fresnel and Fraunhofer approximations in order to reduce the spherical wavefronts of point sources on the aperture to planar wavefronts once they reach the sensor. This approximation has strong validity when your sensor is in the far field, or alternatively when a lens is used to focus light onto the sensor. Through this simplification, the PSF can be found by analyzing the Fraunhofer diffraction pattern, which is proportional to the

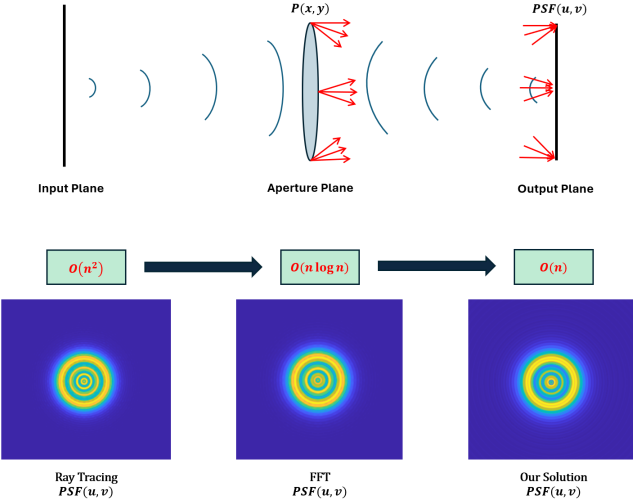


Fig. 1. (Top) PSF Formation Diagram. In the ray tracing technique, each point on the aperture plane is treated as the source of an expanding spherical wave. Then, by exhaustively summing the contributions from each source at each point on the sensor, the PSF can be computed. In the Fresnel Integral, analyzing the transformations taken by the light wave as it propagates through a lens and free space leads the PSF approximately equal to the Fourier transform of a phase-distorted aperture function. Although less accurate than ray tracing, the Fresnel approach is significantly more efficient to compute. (Bottom) Comparison of PSF Computation Methods and their time complexity. For a 1D system, ray tracing requires $O(n^2)$ and through the FFT algorithm the Fresnel technique requires $O(n \log n)$. However, for large n , even the FFT can struggle to keep up with live image processing demand.

Fourier transform of the pupil function of your optical system [2][3]. The pupil or aperture function describes the ways in which light is modified as it passes through the aperture or lens of the system and often includes aberration terms as a result non-ideal artifacts in the optical system or scene [5]. In practice, these aberrations manifest as distortions in the final image, and incorporating them into the pupil function provides a more realistic and accurate PSF. Two of the most common aberrations modeled are defocus and spherical. Defocus is present whenever scenes are imaged outside the plane of focus and leads to an expanded PSF. The severity of this aberration depends on how misaligned the object or sensor is from its focal plane. The spherical aberration is an optical issue which arises as a result of lens imperfections, namely the spherical nature of lenses, and leads to non-ideal imaging as light rays farther from the optical axis tend to focus at different points than those near the center. Although the approximations in Fraunhofer diffraction hinder the accuracy of the result, the gain in computational speed often outweighs the drawbacks. In current ISP and computer vision

systems, which often rely on Fraunhofer diffraction and the Fourier transform of the pupil, the PSF is typically obtained by employing the Fast Fourier Transform (FFT) algorithm, which has a 1D time complexity of $O(n \log n)$ [5]. This is a significant improvement from the cost of applying the Huygen-Fresnel principle. Yet, when this essential calculation is performed for large n or on many images, particularly in applications that require real-time image processing such as automation, medical imaging, or surveillance, the FFT can be a bottleneck for processing and reduce the overall speed of imaging systems. With an increasing number of applications employing real-time vision, the need to further reduce computation of PSFs is crucial.

In this paper, we develop a set of approximations of the Fourier-Bessel transform, which lead to a closed-form solution for the PSF of defocused pupil functions, in order to have the PSF computation run as $O(n)$. We demonstrate the validity of the approximations over a range of defocus strengths and spatial extents in the image plane, ensuring that the method is robust across different imaging scenarios. We also demonstrate how this result can be extended to apply to spherical aberrations through a piecewise expression of the spherical aberration term. These results have the potential to accelerate image processing, especially in live-scene capture, where speed is often the limiting factor for system usability and image quality. Finally, these results may serve as a starting point for future work in acceleration of computational imaging, particularly for other kinds of aberrations.

2. PRINCIPLE

One of the most researched and important radially symmetric aberrations is defocus, which plays a critical role in depth-from-focus or defocus computer vision techniques. Defocus arises as a result of the sensor plane being misaligned with the image plane of an optical system. The impact of defocus on the distribution of light at the sensor can be derived through the analysis of lens distortion and free-space wave propagation. From Goodman's derivation, the distribution of an optical field following propagation through a distance z in free space is given by the Fresnel Diffraction Integral [5]. So, given an impulse in the object plane, (x, y) , the field impulse response at the sensor plane, (u, v) , is given by 1, where we account for the the first occurrences of propagation in free space through distance z_1 , the phase distortion caused by the lens, and the final propagation through distance z_2 .

$$U(u, v) = \frac{e^{j k z}}{\lambda z_1 z_2} e^{j \frac{k}{2z_2} (u^2 + v^2)} \cdot \mathcal{F} \left\{ A(x, y) e^{j \frac{k}{2} \left(\frac{1}{z_1} + \frac{1}{z_2} - \frac{1}{f} \right) (x^2 + y^2)} \right\} \quad (1)$$

Here, the Fourier transform variables are given by $f_x = \frac{u}{\lambda z_2}$ and $f_y = \frac{v}{\lambda z_2}$. The aperture function, $A(x, y)$, defines the spatial extent of the lens and f is the focal distance of the lens. When the imaging law, $\frac{1}{z_1} + \frac{1}{z_2} = \frac{1}{f}$, is satisfied, the intensity distribution of the impulse response at the sensor will be proportional to the magnitude square of the transformed aperture function. When the imaging law is not satisfied, the argument of the Fourier transform obtains a quadratic phase distortion of the form

$$\Phi_{\text{defocus}}(R) = C_d \frac{2(x^2 + y^2)}{(x^2 + y^2)_{\max}} \quad (2)$$

with

$$C_d = \frac{\pi}{2\lambda} \left(\frac{1}{z_1} + \frac{1}{z_2} - \frac{1}{f} \right) (x^2 + y^2)_{\max} \quad (3)$$

The defocus constant C_d signifies the strength of defocus in the system. With this, we define the argument of the Fourier transform in 1 as the pupil function, $P(R) = A(R) \exp[j\Phi_{\text{defocus}}]$, and note its transform as 4 after converting the Fourier integral to polar coordinates.

$$\begin{aligned} \mathcal{F}\{P(R, \theta)\}(k, \phi_k) = \\ \int_0^{2\pi} \int_0^{R_{\max}} \exp[i\Phi(R, \theta)] \cdot \exp[-ikR \cos(\theta - \phi_k)] R dR d\theta \end{aligned} \quad (4)$$

Here, we have $k = \sqrt{f_x^2 + f_y^2}$ and $\phi_k = \tan^{-1} \frac{f_y}{f_x}$ and $R = \sqrt{x^2 + y^2}$ and $\theta = \tan^{-1} \frac{y}{x}$ being variables representing the radial distance from the optical axis and the azimuthal angle in sensor plane and aperture plane, respectively [5]. Further, R_{\max} represents the maximum radius of the aperture over which light is collected.

For radially symmetric pupil functions, including ones distorted by defocus, we can reorder the integrals and define the Bessel function of the first kind, zero order J_0 [5]. It is also noteworthy to mention that as a direct result the pupil function having no θ dependence, its transform and resulting PSF will correspondingly have no dependence on ϕ . In other words, a radially symmetric pupil function will lead to a radially symmetric PSF. After defining the Bessel function, J_0 , we can write 4 as 5.

$$2\pi \int_0^{R_{\max}} \exp \left[j \frac{2C}{R_{\max}^2} \cdot R^2 \right] J_0(2\pi kR) R dR \quad (5)$$

With the aim of developing an approximation for the integrand in 5, we introduce 2 alternate expressions for J_0 . Both given by Abramowitz and Stegun in the Handbook of Mathematical Functions, the first is the infinite series in

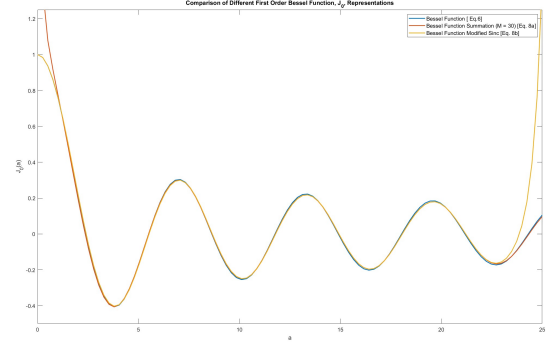


Fig. 2. Comparison of Various Forms of $J_0(a)$

6, and the second is the closed form approximation which grows stronger as the argument becomes large as shown in 7 [6]. A comparison of the various representations of a one-dimensional Bessel Function is shown in Figure 2.

$$J_0(a) = \sum_{m=0}^{\infty} \frac{(-1)^m}{(m!)^2} \left(\frac{a}{2} \right)^{2m} \quad (6)$$

$$J_0(a) \approx \sqrt{\frac{2}{\pi a}} \cos(a - \frac{\pi}{4}) \quad (7)$$

At this point, we seek a piecewise approximated representation of $J_0(2\pi kR)$ in order to have the integrand solely contain products of complex exponentials and odd powers of R . The piecewise approximation utilizes the two forms of J_0 listed in 6 and 7, using the first three terms of the infinite summation for values of R near zero and transitions to 7 for larger values of R . For simplicity, in this paper, the transition point was set to where the argument of the Bessel function equals unity, i.e. $2\pi kR = 1$, $R = \frac{1}{2\pi k}$. As expected, the optimal transition point depends heavily on the distance from the optical axis on the image plane, k .

$$J_0(2\pi kR) \approx \begin{cases} 1 - \frac{(2\pi kR)^2}{4} + \frac{(2\pi kR)^4}{64} & \text{if } R \leq \frac{1}{2\pi k} \\ \sqrt{\frac{2}{\pi(2\pi kR)}} \cos(2\pi kR - \frac{\pi}{4}) & \text{if } R > \frac{1}{2\pi k} \end{cases} \quad (8)$$

To simplify the square root term that comes as a result of substituting 7, we apply the approximation in 9, where $\frac{1}{R}$ is approximated as the sum of a line tangent to $\frac{1}{R}$ at $R = \alpha$, $TL(\alpha)$, and the term $\frac{1}{R}$. Variables A and B are the constant values necessary to obtain the tangent line centered at α , and can be found with the closed form expression in 10 and 11.

$$\frac{1}{\sqrt{2\pi kR}} \approx TL(\alpha) + \frac{1}{2\pi kR} = A(\alpha) \cdot 2\pi kR + B(\alpha) + \frac{1}{2\pi kR} \quad (9)$$

$$A(\alpha) = -\frac{1}{2} \alpha^{-\frac{3}{2}} \quad (10)$$

$$B(\alpha) = \frac{3}{2\sqrt{\alpha}} \quad (11)$$

The resulting integrand is summarized in 12. It is defined piece wise, replacing the integral definition of $J_0(2\pi kR)$ with the first 3 terms of the 6 for values of $R \leq \frac{1}{2\pi k}$, and with 7 and 9 for values of $R > \frac{1}{2\pi k}$. The adjustable parameters following this derivation include the transition point between the two forms of $J_0(2\pi kR)$, the number of terms used in the summation definition of J_0 , and the center of the line tangent to $\frac{1}{\sqrt{2\pi kR}}$, α , when making the approximation in 9. The values of A and B are dependent on the center of the tangent line chosen and are given by 10 and 11.

$$\begin{aligned} \mathcal{F}\{P(R, \theta)\} = 2\pi \left\{ \right. \\ \left. \int_0^{\frac{1}{2\pi k}} \left(1 - \frac{(2\pi kR)^2}{4} + \frac{(2\pi kR)^4}{64} \right) \exp\left[j\frac{2C_d R^2}{R_{\max}^2}\right] R dR \right. \\ \left. + \int_{\frac{1}{2\pi k}}^{R_{\max}} \left(A \cdot 2\pi kR + B + \frac{1}{2\pi kR} \right) \cos\left(2\pi kR - \frac{\pi}{4}\right) \right. \\ \left. \cdot \exp\left[j\frac{2C_d R^2}{R_{\max}^2}\right] R dR \right\} \quad (12) \end{aligned}$$

The first integral covering values of R from 0 to $\frac{1}{2\pi k}$ is solvable with integration by parts. The second integral, after using Euler's Identity to split the cosine term into 2 complex exponentials has a known closed form solution after applying both integration by parts and the integral 7.4.32 from Abramowitz and Stegun repeated in 13 [6].

$$\begin{aligned} \int \exp[-(ax^2 + 2bx + c)] dx = \\ \frac{1}{2} \sqrt{\frac{2}{a}} \exp\left[\frac{b^2 - ac}{a}\right] \operatorname{erf}\left[\sqrt{a}x + \frac{b}{\sqrt{a}}\right] + \text{constant} \quad (13) \end{aligned}$$

The full result of the integrals can be found in the Appendix. Taking the norm square of this result will give the PSF of the pupil function. The final consideration which must be given is the presence of the error function, erf, which receives complex arguments present in the final integral solution. Current implementations of erf with complex functionality are computationally and time expensive, greatly increasing the time necessary to calculate a PSF. As a result, we look to Abramowitz and Stegun to develop an approximated version of erf in 14 which can handle complex inputs without significant time consumption [6]. The approximation in 14 improves as N grows larger, as a result N is another parameter which impacts accuracy and error.

$$\begin{aligned} \operatorname{erf}[x + jy] \approx \operatorname{erf}[x] + \frac{\exp[-x^2]}{2\pi x} [(1 - \cos 2xy) + j \sin 2xy] \\ + \frac{2}{\pi} \exp[-x^2] \sum_{n=1}^N \frac{\exp[-\frac{n^2}{4}]}{n^2 + 4x^2} [f_n(x, y) + j g_n((x, y))] \quad (14) \end{aligned}$$

with

$$f_n(x, y) = 2x - 2x \cosh(ny) \cos(2xy) + n \sinh(ny) \sin(2xy)$$

$$g_n(x, y) = 2x \cosh(ny) \sin(2xy) + n \sinh(ny) \cos(2xy)$$

3. RESULTS

Next, we present direct comparisons between the PSF calculated with the aforementioned closed form integral solution (CFIS) and the 2D FFT algorithm. Unless indicated otherwise, the following parameters are set to a resolution of 512x512, $R_{\max} = 0.0015$, $\alpha = 100$ (tangent line center).

The outer rings at the edges of the image plane are a direct result of the approximated erf function in 14 and the strength of the rings can be reduced by increasing the number of summation terms, N . Since the result from the FFT shows a monotonically decreasing PSF after the final ring, one can consider truncating the rest of the PSF values to zero beyond a set R value. In doing so, the outer rings will no longer appear and further error can be reduced.

5 shows MSE between the closed form solution and the FFT algorithm for varying values of N . These three plots show some key results. First, increasing N decreases the intensity of the outer rings, which can bring down the MSE to 0.0009 at $N = 30$, $C_d = 10$, and $\alpha = 100$. Second, it also shows how most error is concentrated in the center of the 2D PSF when the defocus strength is relatively low. This result can be seen more clearly in the 1D slice representation in ??, where the peak error is 0.368.

Next, increasing the strength of defocus in the system expands the PSF as expected. This expansion leads to greater error for larger k as the approximation of $\frac{1}{2\pi kR}$ in 9 weakens. To correct this, we can shift the tangent line center (TLC) by increasing α to better match values at high k . Doing so comes at the tradeoff of worsening the approximation for lower k as seen in the increased error at the inner rings of 7 as α increases to 200. Despite this, the overall MSE reduces from 0.0196 to 0.00199 when properly shifting the TLC to a greater value.

4. DISCUSSION

As a whole, the approximations made in the derivation of the closed form solution are shown to result in a reasonable error across a broad range of defocus strengths. Additionally, by fine-tuning the parameters listed in the derivation, the error

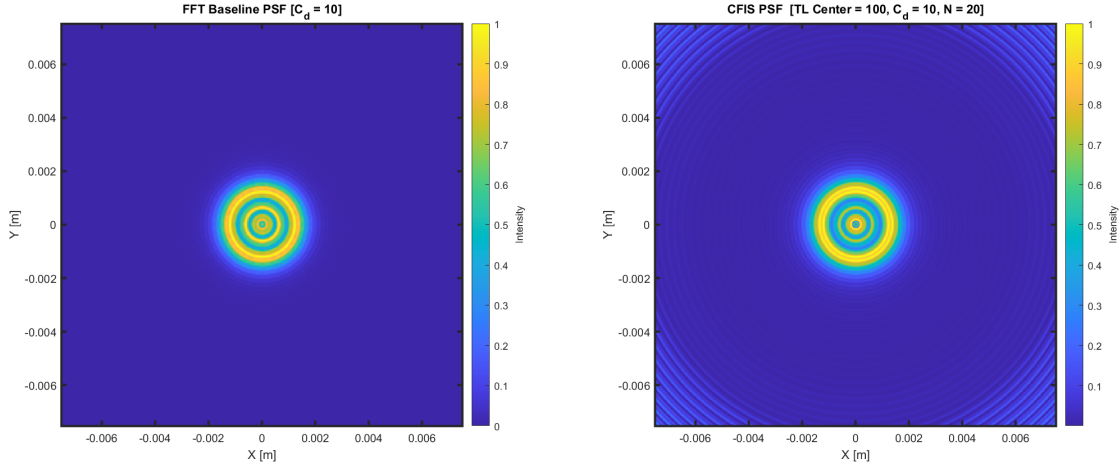


Fig. 3. PSF Comparison between FFT and CFIS

between the integral solution of the PSF given some defocus value and the FFT result can be further reduced. This flexibility allows the approach to be adapted to different imaging systems or operating conditions, making it useful in both scientific imaging and computer vision pipelines.

A few limitations of this solution also revolve around the mathematical approximations made in this paper. First, as the strength of defocus grows large, there will be an increasingly costly trade-off between error in the center of the PSF and the error at the outer rings of the PSF. This is because the approximation in 9 is generally not suited for a very wide range of values. Furthermore, the approximation of the erf function in 14 is still the most time-consuming component of the computation and still results in error as shown through the rings in 5. Using a lookup table to implement a complex erf is a potential solution to this problem.

The reduction in computational complexity can lead to significant improvements in speed within live image processing, especially when high-resolution images are used or spatially varying PSFs must be computed. In particular, applications such as real-time microscopy, astronomical imaging, and embedded vision systems stand to benefit, as these systems often require fast and repeated PSF evaluations under narrow time windows.

This solution can also be expanded to the spherical aberration, which following the Zernicke polynomial model is represented in the pupil function by including the complex phase term in 15, with C_s representing the degree of strength of the spherical aberration.

[7].

$$\phi_{\text{spherical}}(R) = \exp \left[iC_s \frac{R^4}{R_{\max}^4} \right] \quad (15)$$

A pupil function with both spherical and defocus aberrations is then fully described by 16. However, the presence of the quartic term R^4 within the exponential makes it significantly more challenging to apply the same procedure as before or even find similar approximations. So, our approach is to split the pupil function piecewise into N quadratic exponentials with parameters α_i and β_i as in 17, each valid only within the range $[R_i, R_{i+1})$ and apply the closed form solution in the previous section to each to solve for the PSF. With this method, we save computation time by splitting the pupil function more coarsely than the FFT algorithm, allowing for less total iterations and steps.

$$P(R) = \exp \left[i(C_d \frac{2R^2}{R_{\max}^2} - 1) + iC_s \frac{R^4}{R_{\max}^4} \right] \quad (16)$$

The process of finding the optimal values of α_i and β_i for each quadratic exponential in 17 can be presented as an optimization problem with 4 inputs (C_d, C_s, R_i, R_{i+1}) and 2 outputs (α, β). A rudimentary alternative to this problem is to sweep over a large set of α and β values and calculate the error between the corresponding quadratic exponential and the quartic exponential to choose the set of $\{\alpha, \beta\}$ with the least error. This method can provide accurate constructions of the true pupil function with as little as 5 quadratic exponentials with a total mean squared error of 0.000137.

$$P(R) = \exp \left[i \left(C_d \left(\frac{2R^2}{R_{\max}^2} - 1 \right) + C_s \frac{R^4}{R_{\max}^4} \right) \right]$$

↓

$$P(R) = \begin{cases} e^{i[\alpha_1 R^2 + \beta_1 R]} & 0 \leq R < R_1 \\ e^{j[\alpha_2 R^2 + \beta_2 R]} & R_1 \leq R < R_2 \\ \vdots \\ e^{j[\alpha_N R^2 + \beta_N R]} & R_{N-1} \leq R < R_N \end{cases} \quad (17)$$

Additionally, further accuracy can be obtained by adjusting the way in which the quadratic exponentials are split. The simplest method of splitting bounds linearly such that $R_1 = 1 \cdot \frac{R_m}{N}$, $R_2 = 2 \cdot \frac{R_m}{N}, \dots, R_i = i \cdot \frac{R_m}{N}$ can improved by recognizing finer splits will be required as R approached R_{\max} as a result of an accelerating increase in phase in the complex exponential due to R^4 and R^2 terms. Altering split lengths for each quadratic exponential and reducing the length for larger i values by using a square root or log function to determine length could further reduce error.

5. CONCLUSION

Reducing computation time for optical imaging systems remains a top priority for real time applications and processing of live scenes. By having an PSF computation run as $O(n^2)$ instead of $O(n^2 \log n)$ with an approximated closed form solution that maintains strong accuracy, we can improve performance and speed in fields such as object tracking/detection, video capture, and pattern recognition. Future research should be focused on further optimizing parameters listed in this paper and expanding on functionality by finding closed form solutions for non-radially symmetric aberrations including coma, astigmatism, and trefoil.

6. APPENDIX

6.1. Closed Form Integral Solution.

Let the following variables be defined as

$$\alpha = \frac{2C_d}{R_{\max}^2}$$

$$\beta = 2\pi k$$

Define A_{tl} and B_{tl} as the tangent line variables defined by 10 and 11, respectively. $T = \frac{1}{2\pi k}$ as the transition point between the 2 forms of J_0 defined in 6 and 7. We can split the full integral in 12 into the sum of the following 6 sub-integrals.

$$1. \int_0^T \exp [i\alpha R^2] R dR$$

2. $- \int_0^T \frac{(\beta R)^2}{4} \exp [i\alpha R^2] R dR$
3. $\int_0^T \frac{(\beta R)^4}{64} \exp [i\alpha R^2] R dR$
4. $\int_T^{R_{\max}} A_{tl} (\beta R) \cos (\beta R - \frac{\pi}{4}) \exp [i\alpha R^2] R dR$
5. $\int_T^{R_{\max}} B_{tl} \cos (\beta R - \frac{\pi}{4}) \exp [i\alpha R^2] R dR$
6. $\int_T^{R_{\max}} \frac{1}{\beta R} \cos (\beta R - \frac{\pi}{4}) \exp [i\alpha R^2] R dR$

After applying a substitution for R^2 and using integration by parts for integrals 1, 2, and 3 you will arrive at the at the solutions listed in 18, 19, and 20.

$$\frac{1}{2i\alpha} [e^{i\alpha T^2} - 1] \quad (18)$$

$$\frac{-(\beta)^2}{8} \left[\frac{e^{i\alpha T^2}}{\alpha^2} - \frac{iT^2 e^{i\alpha T^2}}{\alpha} - \frac{1}{\alpha^2} \right] \quad (19)$$

$$\frac{(\beta)^4}{128} \left[- \frac{(i\alpha^2 T^4 - 2\alpha T^2 - 2i) e^{i\alpha T^2}}{\alpha^3} - \frac{2i}{\alpha^3} \right] \quad (20)$$

For integrals 4, 5, and 6, splitting the cosine term into 2 complex exponentials with Euler's Identity, and again applying integration by parts along with the result in 13 will result in the solutions in 21, 22, and 23. Finally, the PSF can be found by taking the norm square of the sum of 18 to 23 and multiplying by $4\pi^2$.

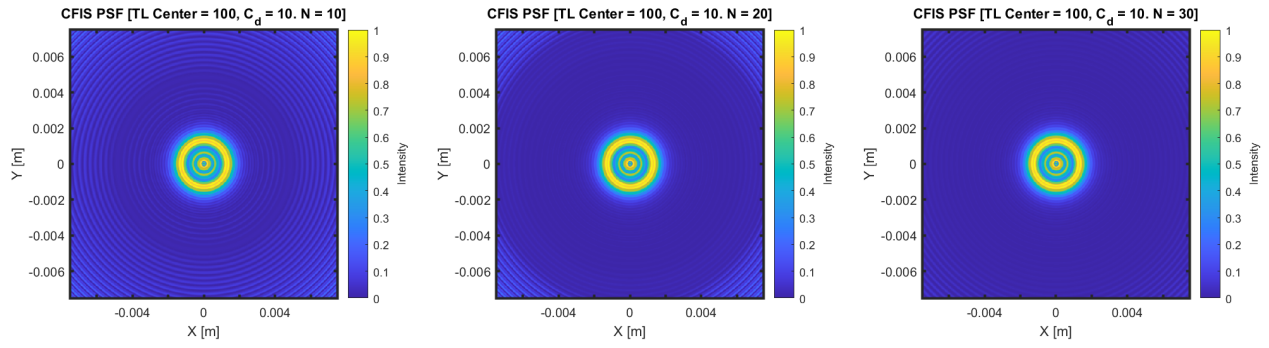


Fig. 4. CFIS PSF for Varying N Values

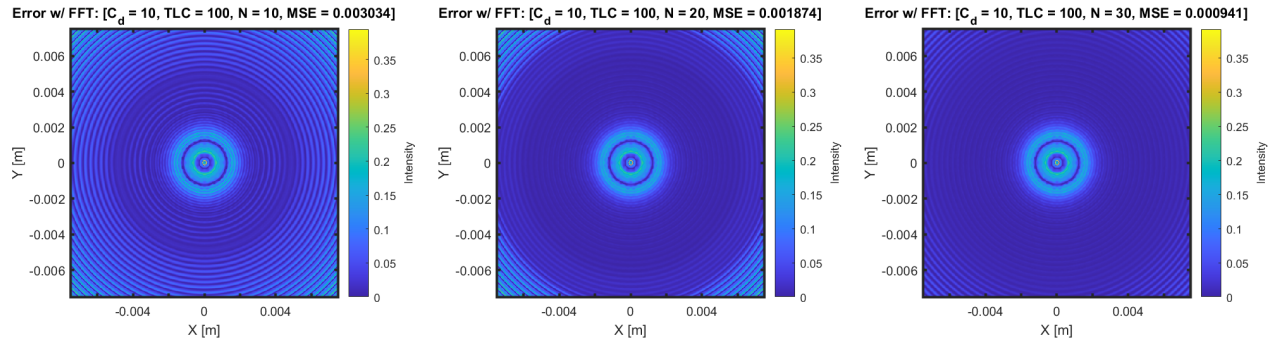


Fig. 5. Error Between CFIS PSF and FFT for Varying N Values

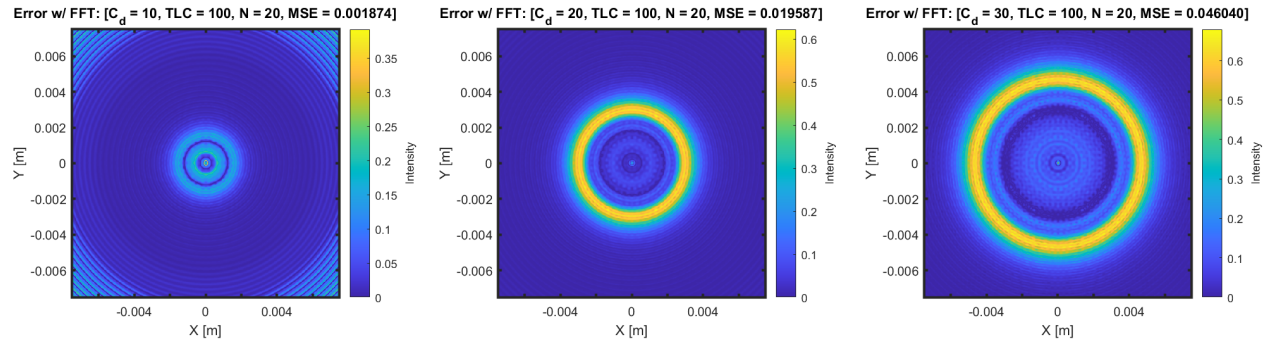


Fig. 6. Error Between CFIS PSF and FFT for Varying Defocus Values

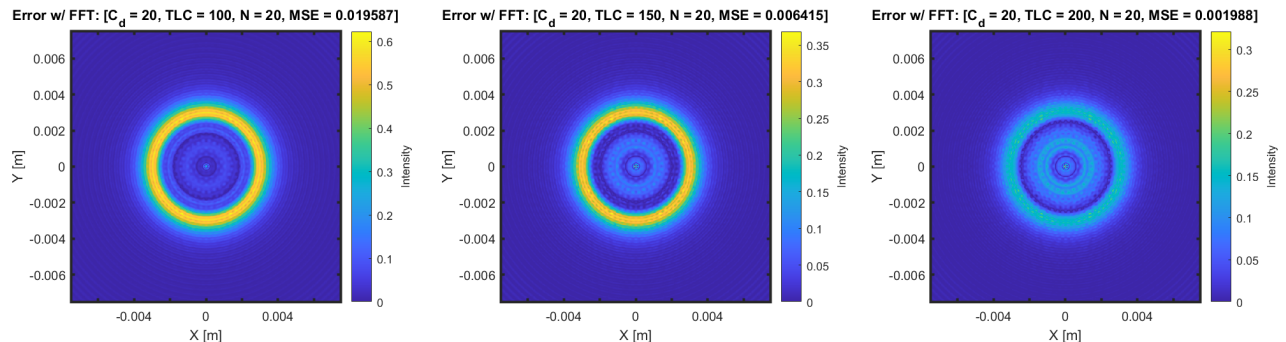


Fig. 7. Error Between CFIS PSF and FFT for Varying Tangent Line Centers (TLC)

Equation 21 is below.

$$\begin{aligned}
& \frac{A_{tl}\beta}{16\alpha^3} e^{-\frac{i\pi}{4}} e^{-\frac{i\beta^2}{4\alpha}} \left[(-1)^{\frac{3}{4}} \sqrt{\pi\alpha} (\beta^2 + 2i\alpha) \operatorname{erfi} \left(\frac{(-1)^{\frac{1}{4}} (2\alpha R_{max} + \beta)}{2\sqrt{\alpha}} \right) \right. \\
& + 2i\alpha (2\alpha R_{max} - \beta) e^{\frac{i(2\alpha R_{max} + \beta)^2}{4\alpha}} - (-1)^{\frac{3}{4}} \sqrt{\pi\alpha} (\beta^2 + 2i\alpha) \operatorname{erfi} \left(\frac{(-1)^{\frac{1}{4}} (2\alpha T + \beta)}{2\sqrt{\alpha}} \right) \\
& \left. + 2i\alpha (2\alpha T - \beta) e^{\frac{i(2\alpha T + \beta)^2}{4\alpha}} \right] + \\
& \frac{A_{tl}\beta}{16\alpha^3} e^{+\frac{i\pi}{4}} e^{-\frac{i\beta^2}{4\alpha}} \left[(-1)^{\frac{3}{4}} \sqrt{\pi\alpha} (\beta^2 + 2i\alpha) \operatorname{erfi} \left(\frac{(-1)^{\frac{1}{4}} (2\alpha R_{max} - \beta)}{2\sqrt{\alpha}} \right) \right. \\
& + 2i\alpha (2\alpha R_{max} + \beta) e^{\frac{i(2\alpha R_{max} - \beta)^2}{4\alpha}} - (-1)^{\frac{3}{4}} \sqrt{\pi\alpha} (\beta^2 + 2i\alpha) \operatorname{erfi} \left(\frac{(-1)^{\frac{1}{4}} (2\alpha T - \beta)}{2\sqrt{\alpha}} \right) \\
& \left. + 2i\alpha (2\alpha T + \beta) e^{\frac{i(2\alpha T - \beta)^2}{4\alpha}} \right] \tag{21}
\end{aligned}$$

Equation 22 is below.

$$\begin{aligned}
& \frac{\beta}{2} e^{-i\pi/4} \left[\frac{\sqrt{\pi} i\beta e^{-\frac{i\beta^2}{4\alpha}}}{4\sqrt{i}\alpha^{3/2}} \operatorname{erf} \left(\frac{i^{3/2} (2\alpha R_{max} + \beta)}{2\sqrt{\alpha}} \right) - \frac{i e^{i\alpha R_{max}^2 + i\beta R_{max}}}{2\alpha} \right. \\
& - \frac{\sqrt{\pi} i\beta e^{-\frac{i\beta^2}{4\alpha}}}{4\sqrt{i}\alpha^{3/2}} \operatorname{erf} \left(\frac{i^{3/2} (2\alpha T + \beta)}{2\sqrt{\alpha}} \right) + \frac{i e^{i\alpha T^2 + i\beta T}}{2\alpha} \left. \right] \\
& + \frac{\beta}{2} e^{+i\pi/4} \left[- \frac{\sqrt{\pi} i\beta e^{-\frac{i\beta^2}{4\alpha}}}{4\sqrt{i}\alpha^{3/2}} \operatorname{erf} \left(\frac{i^{3/2} (2\alpha R_{max} - \beta)}{2\sqrt{\alpha}} \right) \right. \\
& - \frac{i e^{i\alpha R_{max}^2 - i\beta R_{max}}}{2\alpha} + \frac{\sqrt{\pi} i\beta e^{-\frac{i\beta^2}{4\alpha}}}{4\sqrt{i}\alpha^{3/2}} \operatorname{erf} \left(\frac{i^{3/2} (2\alpha T - \beta)}{2\sqrt{\alpha}} \right) + \frac{i e^{i\alpha T^2 - i\beta T}}{2\alpha} \left. \right] \tag{22}
\end{aligned}$$

Equation 23 is below.

$$\begin{aligned}
& \frac{1}{2\beta} e^{-\frac{\pi}{4}} \left[\frac{-\sqrt{\pi} i e^{-\frac{i\beta^2}{4\alpha}}}{2\sqrt{i}\sqrt{\alpha}} \operatorname{erf}\left(\frac{i^{3/2}(2\alpha R_{max} + \beta)}{2\sqrt{\alpha}}\right) \right. \\
& - \frac{-\sqrt{\pi} i e^{-\frac{i\beta^2}{4\alpha}}}{2\sqrt{i}\sqrt{\alpha}} \operatorname{erf}\left(\frac{i^{3/2}(2\alpha T + \beta)}{2\sqrt{\alpha}}\right) \left. \right] \\
& + \frac{1}{2\beta} e^{+\frac{\pi}{4}} \left[\frac{-\sqrt{\pi} i e^{-\frac{i\beta^2}{4\alpha}}}{2\sqrt{i}\sqrt{\alpha}} \operatorname{erf}\left(\frac{i^{3/2}(2\alpha R_{max} - \beta)}{2\sqrt{\alpha}}\right) \right. \\
& - \frac{-\sqrt{\pi} i e^{-\frac{i\beta^2}{4\alpha}}}{2\sqrt{i}\sqrt{\alpha}} \operatorname{erf}\left(\frac{i^{3/2}(2\alpha T - \beta)}{2\sqrt{\alpha}}\right) \left. \right]
\end{aligned} \tag{23}$$

7. REFERENCES

- [1] H. Ikoma, C. M. Nguyen, C. A. Metzler, Y. Peng, and G. Wetzstein, “Depth from defocus with learned optics for imaging and occlusion-aware depth estimation,” in *2021 IEEE International Conference on Computational Photography (ICCP)*, Haifa, Israel, 2021, pp. 1–12, IEEE.
- [2] F. Mannan and M. S. Langer, “Blur calibration for depth from defocus,” in *13th Conference on Computer and Robot Vision (CRV)*, Victoria, BC, Canada, 2016, pp. 281–288, IEEE.
- [3] S. Chaudhuri and A. N. Rajagopalan, *Depth from Defocus: A Real Aperture Imaging Approach*, Springer-Verlag, New York, 1 edition, 1999.
- [4] Neel Joshi, Richard Szeliski, and David J. Kriegman, “Psf estimation using sharp edge prediction,” in *2008 IEEE Conference on Computer Vision and Pattern Recognition*, 2008, pp. 1–8.
- [5] J. Goodman, *Fourier Optics*, McGraw-Hill, New York, 2 edition, 1996.
- [6] M. Abramowitz and I. A. Stegun, *Handbook of Mathematical Functions with Formulas, Graphs, and Mathematical Tables*, U.S. Dept. of Commerce, 9 edition, 1964.
- [7] R. J. Mathar, “Zernike basis to cartesian transformations,” *Serbian Astronomical Journal*, , no. 179, pp. 107–120, 2009.